Adaptive Microwave Photonic Multi-Coset Sampling With Optimized Sampling Pattern

Xiaohu Tang, Yuxiang Cai, Ping Li, Yamei Zhang, *Member, IEEE*, and Shilong Pan, *Fellow, IEEE*

***Abstract*—An adaptive microwave photonic multi-coset sampling (MCS) method is proposed to enable accurate and efficient sub-Nyquist acquisition of multiband radio frequency (RF) signals. The method integrates an activated Nyquist band sensor and a sampling pattern optimization module to dynamically optimize the sampling pattern based on prior spectral knowledge. The activated Nyquist band sensor can efficiently estimate the prior spectral support. A fine microwave frequency-sweeping technique is introduced to characterize both the sampling pattern and the measurement matrix, enabling precise calibration and control of the relative time delays in the sampling channels. A four-channel, 1-GSa/s microwave-photonic MCS system is implemented and experimentally validated. Multiband signals spanning four and eight distinct Nyquist bands across 0.01–40 GHz with a cumulative bandwidth of 2 GHz are adaptively sampled and successfully reconstructed. The proposed method demonstrates the ability to achieve the theoretical minimum sampling rate while maintaining a well-conditioned measurement matrix through optimized sampling pattern design. The experimental results further reveal that the system is robust to spectral aliasing and capable of resolving prealiasing components under limited sampling channels. This work represents, to the best of our knowledge, the first hardware demonstration of an adaptive microwave photonic multi-coset sampler with full-band sensing and sampling pattern control. Owing to its simple architecture, low sampling rate, and adaptability, the proposed system offers a promising solution for next-generation multiband RF front ends, particularly in applications such as multiband radar, wideband spectrum sensing, and cognitive radio.**

***Index Terms*—Microwave photonics, multicoset sampling (MCS), sampling pattern optimization, spectrum sensing.**

I. Introduction

With the rapid advancements in radar, communications, and wideband spectrum sensing, the demand for efficient radio frequency (RF) signal acquisition has grown increasingly critical [1]. Multiband RF signals, as a fundamental signal model, are widely used in multiband radar [2], multicarrier communications [3], and cognitive radio systems [4]. Among the various receiver schemes, the superheterodyne receiver is the most widely used [5]. However, the RF front-end complexity grows with the number of frequency bands, presenting significant challenges for multiband RF signal processing as the band count increases. Benefiting from advanced digital technology, wideband sampling techniques have been extensively adopted for high-frequency signal acquisition [6]. However, these methods require high-bandwidth, high-sampling-rate analog-to-digital converters (ADCs), leading to significant hardware costs and data redundancy.

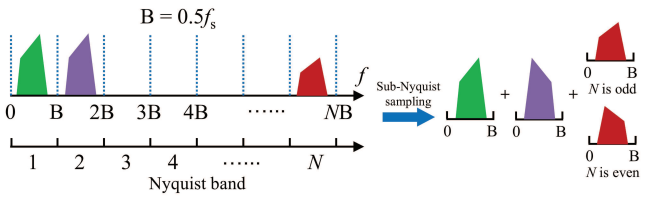

Fig. 1. Illustration of the multiband signal, sub-Nyquist sampling, and frequency folding.

To reduce data redundancy, compressed sampling has emerged as an effective acquisition approach [7], [8]. It can be broadly categorized into random demodulation (RD) [9], modulated wideband converter (MWC) [10], and multicoset sampling (MCS) [11]. RD and MWC employ high-speed random modulation to fold the spectrum into a low-frequency range, enabling reconstruction via compressed sensing algorithms. These methods demand high-speed random pseudorandom binary sequence (PRBS) covering the entire Nyquist bandwidth, increasing the hardware implementation complexity. In contrast, MCS operates without external randomness. It employs multiple sub-Nyquist sampling channels with distinct time delays, folding the wideband multiband signal spectrum into the first Nyquist band. Fig. 1 illustrates the sub-Nyquist sampling process and the frequency-folding effect.

Due to the low cost and simple structure, MCS has been extensively studied at the theory level [12], [13], [14], [15]. However, practical hardware implementations are rare due to several key challenges. First, MCS inherently introduces spectral aliasing, requiring the identification of the original Nyquist band for each aliased frequency. Traditional methods, such as the continuous-to-finite (CTF) module in compressed sensing [16], estimate spectral support via matrix decomposition. These approaches are only effective when numerous sampling channels and signal sparsity assumptions are met, limiting their applicability and hardware feasibility. Second, the MCS reconstruction accuracy heavily depends on the sampling pattern, which is determined by the relative

Received 11 April 2025; revised 29 June 2025; accepted 9 July 2025. Date of publication 24 July 2025; date of current version 26 November 2025. This work was supported in part by the Innovation Capacity Building Plan (Science and Technology Facilities) of Jiangsu under Grant BM2022017 and in part by the Fundamental Research Funds for the Central Universities under Grant NI023003. *(Corresponding author: Yamei Zhang.)*

The authors are with the National Key Laboratory of Microwave Photonics, Nanjing University of Aeronautics and Astronautics, Nanjing 210016, China (e-mail: tangxiaohu@nuaa.edu.cn; cai_yuxiang@nuaa.edu.cn; li_ping@nuaa.edu.cn; zhang_ym@nuaa.edu.cn; pans@nuaa.edu.cn).

Digital Object Identifier 10.1109/TMTT.2025.3588746

sampling time delays between channels [17]. It remains a major challenge in electronic systems to achieve wide-range, high-speed, and high-precision relative sampling time delay control. Additionally, to ensure accurate reconstruction, the measurement matrix should be well-conditioned, thus requiring careful sampling pattern design. Conventional sampling pattern design methods [17], [18], [19], primarily based on compressed sensing principles, aim to design a measurement matrix that follows the restricted isometry property (RIP), which is a nondeterministic polynomial-time hard (NP-hard) problem. Furthermore, most existing methods constrain the relative sampling time delays to integer multiples of the Nyquist sampling period, reducing adaptability and flexibility [20].

Over the past few decades, advancements in microwave-photonic technologies have enabled wideband instantaneous frequency measurement and high-precision, fast optical time delay measurement [21], [22], [23]. Moreover, microwave-photonic sub-Nyquist sampling techniques have been successfully applied to radar signal reception [24] and wideband spectrum sensing [25], [26], offering a promising platform for MCS implementation. In [27], an effective single-channel implementation of microwave-photonic-based MCS was demonstrated. The system used a pulse-picked periodic nonuniform optical pulse train to achieve high-fidelity reconstruction of multiband signals over a 5-GHz instantaneous bandwidth. However, it relies on a high-speed PRBS for pulse selection and requires a broadband track-and-hold amplifier for pulse tracking and holding. Additionally, as a single-channel system, it requires a uniformly sampled ADC to acquire nonuniformly sampled pulses, leading to data redundancy. To deal with this issue, an MCS with dual low-rate optical pulses was proposed in [28], demonstrating successful reconstruction of multiband signals with a cumulative bandwidth of 600 MHz in numerical simulations. Though the system provides a feasible approach for photonic-based MCS, its experimental validation remains lacking, leaving uncertainties about practical limitations like scalability and real-world performance. In addition, all the previously reported approaches lack adaptive capability and rely on noise-sensitive algorithms for spectral support estimation, seriously limiting their robustness in dynamically varying signal environments.

In this article, to the best of our knowledge, the first hardware implementation of a microwave photonic multi-coset sampler with adaptability based on multichannel sub-Nyquist sampling is proposed and demonstrated. The proposed system consists of an activated Nyquist band sensor and a microwave photonic multi-coset sampler, which adaptively adjusts the sampling pattern based on prior spectral support to ensure successful multiband signal reconstruction. In the experiments, a four-channel adaptive microwave-photonic MCS system with a sampling rate of 1 GSa/s was demonstrated. Four- and eight-band signals, spanning 0.01–40 GHz with an effective bandwidth of 2 GHz, were adaptively sampled and reconstructed. Additionally, the impact of time delay errors on the condition number of the measurement matrix was analyzed, offering a theoretical foundation for precise sampling pattern control in practical applications.

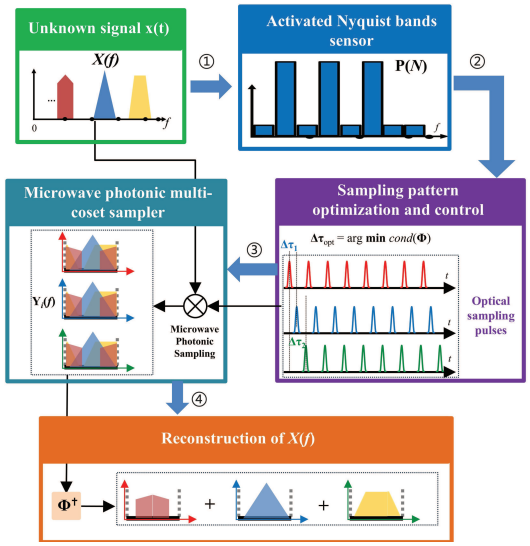

Fig. 2. Workflow of the proposed adaptive microwave-photonic MCS.

II. Principle

The workflow of the proposed adaptive microwave-photonic MCS system is illustrated in Fig. 2. First, the unknown multiband signal is fed into an activated Nyquist band sensor, which divides the Nyquist bandwidth of the signal into N evenly spaced frequency bins. Subsequently, the frequency bins occupied by the signals are identified, thus obtaining the prior spectral support. Since this step requires only modest frequency resolution, a relatively simple implementation can be adopted. Next, based on the prior spectral support, the microwave photonic multi-coset sampler can adaptively optimize the sampling pattern via the sampling pattern optimization and control unit. This step, which is the central focus of this study, ensures that the measurement matrix is well-conditioned, and the sampling procedure is both efficient and targeted. Finally, accurate reconstruction of the multiband signal can be performed in the frequency domain by the signal processing unit, guided by the measurement matrix and prior spectral support. In this section, detailed principles are provided for the microwave photonic multi-coset sampler, the activated Nyquist band sensor, the sampling pattern optimization, and the control unit.

A. microwave photonic multi-coset Sampler

The schematic of the proposed microwave photonic multi-coset sampler is illustrated in the red-dashed region in Fig. 3(a). First, an optical pulse train with a repetition rate of f_s is generated by a mode-locked laser (MLL). This pulse train is subsequently demultiplexed by a demultiplexer (DeMUX) into p branches, each characterized by a distinct wavelength band and assigned optical time delays $\tau_1, \tau_2, \ldots, \tau_p$. Thus, the optical pulses in the ith branch can theoretically be expressed as follows:

$$E_{\text{pulse},i}(t) = \sum_{m=-\infty}^{+\infty} a_i(mf_s)\exp[j2\pi m f_s(t-\tau_i)] \quad (1)$$

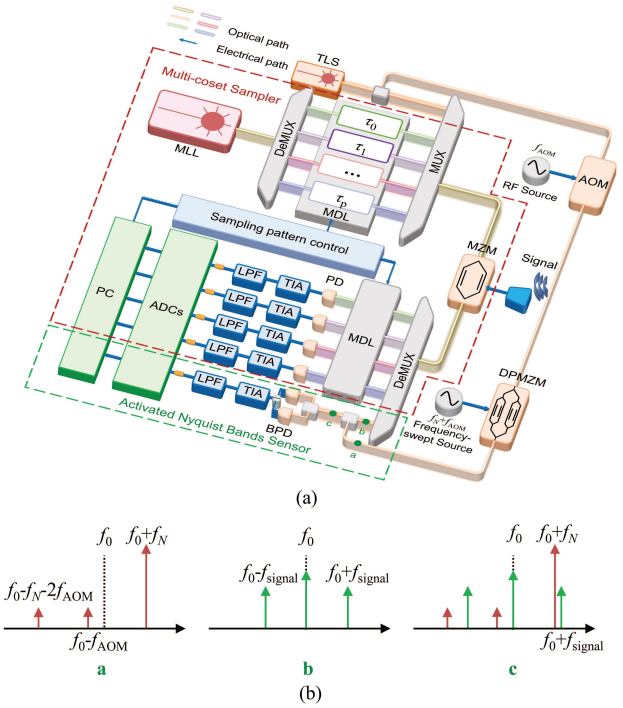

Fig. 3. (a) Schematic of the proposed adaptive microwave photonic multi-coset sampling. MLL: mode-locked laser. TLS: tunable laser source. DeMUX: demultiplexer. MDL: motorized variable optical delay line. MUX: multiplexer. MZM: Mach–Zehnder modulator. AOM: acousto-optic modulator. DPMZM: dual-parallel Mach–Zehnder modulator. PD: photodetector. BPD: balanced PD. TIA: transimpedance amplifier. LPF: low-pass filter. ADC: analog-to-digital converter. PC: personal computer. (b) Illustration of the optical spectra in points a, b, and c.

where m and $a_i(mf_s)$ are the integer index and the coefficients of the pulse train Fourier series, respectively. The optical pulses of the p branches are recombined by a multiplexer (MUX) and then directed into a Mach–Zehnder modulator (MZM) to sample the unknown RF signal $x(t)$. The optical pulses of the ith branch after sampling can be given by

$$E_{\mathrm{MZM},i}(t) = E_{\mathrm{pulse},i}(t)\cos\left(\frac{\pi V_{\mathrm{DC}} + \pi x(t)}{2V_\pi}\right) \tag{2}$$

where V_π and V_{DC} denote the half-wave voltage and the biased voltage of the MZM, respectively. Next, the other DeMUX is performed to demultiplex the optical pulses of the p branches. Considering the different time delays between the p branches after demultiplexing, the output of the photodetector (PD) for the ith branch is

$$i_{\mathrm{PD},i}(t) = \eta\left|E_{\mathrm{pulse},i}\left(t-\tau_i'\right)\cos\left(\frac{\pi V_{\mathrm{DC}} + \pi x\left(t-\tau_i'\right)}{2V_\pi}\right)\right|^2 \tag{3}$$

where η is the responsivity of the PD and τ_i' is the time delay of the ith branch after demultiplexing. Assuming that the MZM is biased at the quadrature transmission point (QTP) with small-signal modulation, (3) can be rewritten as

$$i_{\mathrm{PD},i}(t) \propto \frac{\eta\alpha x\left(t-\tau_i'\right)}{2}\sum_{n=-\infty}^{+\infty} I_i(nf_s)\exp\left[j2\pi nf_s\left(t-\tau_i-\tau_i'\right)\right] \tag{4}$$

where α denotes the loss of the ith branch and $I_i(nf_s)$ is the Fourier coefficient of the electrical spectrum of the optical pulses without modulation. The expression of (4) in the frequency domain can be described as

$$\begin{aligned} i_{\mathrm{PD},i}(f) &\propto X(f)\,e^{-j2\pi f\tau_i'} \\ &\quad * \sum_{n=-\infty}^{+\infty} P_i(nf_s)\,\delta(f-nf_s)e^{-j2\pi nf_s(\tau_i+\tau_i')} \\ &= \sum_{n=-\infty}^{+\infty} P_i(nf_s)\,e^{-j2\pi nf_s\tau_i - j2\pi(f+nf_s)\tau_i'}X(f-nf_s) \end{aligned} \tag{5}$$

where $P_i(nf_s) = \sum_{n=-\infty}^{+\infty} 0.5\eta\alpha I_i(nf_s)$. Following this, the output signal of the PD is amplified and filtered by a transimpedance amplifier (TIA) and an electrical low-pass filter (LPF) with a cutoff frequency of $f_s/2$, respectively. Then, an electrical ADC with a sampling rate of f_s is adopted to digitize the obtained intermediate frequency (IF) signal. The spectrum of the digitalized signal can be given as

$$\begin{aligned} Y_i(f) &= \sum_{n=1}^{+\infty} A_i(nf_s, f)\,e^{j\phi_i(nf_s,f)} \\ &\quad \times X\left[\mathrm{ceil}\left(\frac{n-1}{2}\right)f_s + (-1)^{n-1}f\right], \quad f\in\left[0,\frac{f_s}{2}\right) \end{aligned} \tag{6}$$

where n denotes the integer index of the Nyquist bands and ceil(x) is the smallest integer greater than or equal to x. As indicated by (6), the spectrum of $X(f)$ is folded into the first Nyquist band owing to the frequency-folding effect. $A_i(nf_s, f)$ and $\phi_i(nf_s, f)$ are the weighting coefficients determined by the sampling system, particularly the frequency response of the ith branch, and can be written as

$$\begin{cases} A_i(nf_s,f) = P_i\left[\mathrm{ceil}\left(\dfrac{n-1}{2}\right)f_s\right]H_{\mathrm{OE},i}(f) \\ \phi_i(nf_s,f) = (-1)^{n-1}\left[2\pi\mathrm{ceil}\left(\dfrac{n-1}{2}\right)f_s\tau_i + 2\pi f\tau_i'\right] \end{cases} \tag{7}$$

where $H_{\mathrm{OE},i}(f)$ is the frequency response of the ith branch after demultiplexing, including PD, TIA, LPF, and ADC.

If the activated Nyquist bands of the unknown RF signal are identified to be $\{N_1, N_2, \ldots, N_K\}$, the digitalized spectra of the p branches can be expressed as

$$\mathbf{Y}_{p\times 1}(f) = \Phi_{p\times K}(f)\mathbf{X}_{K\times 1}(f) \tag{8}$$

where $\Phi_{p\times K}(f)$ and $X_{K\times 1}(f)$ are the measurement matrix and spectrum slices of $X(f)$, respectively. The detailed expressions of $\Phi_{p\times K}(f)$ and $X_{K\times 1}(f)$ are shown in (9), at the bottom of the next page. As can be seen from (9), it is obvious that if $p \geq K$ and $\Phi_{p\times K}(f)$ is well-conditioned, (8) can be solved by the pseudoinverse of $\Phi_{p\times K}(f)$, which can be described as

$$\mathbf{X}_{K\times 1}(f) = \Phi_{p\times K}^{\dagger}(f)\mathbf{Y}_{p\times 1}(f). \tag{10}$$

Finally, the spectrum slices of $X(f)$ can be obtained, and notably, these slices are confined within the activated Nyquist bands. By contrast, spectrum slices outside of the activated Nyquist bands are regarded as noise and thus set to zero. The perfect reconstruction of $X(f)$ can be achieved once the spectrum slices are appropriately frequency-shifted and combined.

B. Activated Nyquist Band Sensor

To obtain the prior spectral support of the unknown RF signal, an activated Nyquist band sensor is proposed and shown within the green-dashed region in Fig. 3. A single-frequency optical signal with frequency f_0 is generated by a tunable laser source (TLS). This signal is then split into two branches using an optical coupler (OC). One branch is first frequency-shifted by an acousto-optic modulator (AOM) with a shift frequency of f_{AOM}, which is to prevent carrier interference. Subsequently, the frequency-shifted optical signal enters a dual-parallel MZM (DPMZM), where carrier-suppressed single-sideband (CS-SSB) modulation is applied using a frequency-sweeping signal with a frequency of $f_N + f_{\mathrm{AOM}}$ (where $f_N = Nf_s/2 - f_s/4$, $N \in \mathbb{N}$). Theoretically, the CS-SSB optical signal can be expressed as follows:

$$E_a(t) = E_a e^{j2\pi(f_0+f_N)t} \tag{11}$$

where E_a is the complex amplitude of the optical signal. The optical signal of the other branch is combined with the optical pulses from the p branches using the same MUX due to the wavelength difference and is intensity-modulated by the same MZM. The optical signal modulated at a frequency of f_{signal} can be given as

$$E_b(t) = E_{b,0}e^{j2\pi f_0 t} + E_{b,-1}e^{j2\pi(f_0-f_{\mathrm{signal}})t} + E_{b,1}e^{j2\pi(f_0+f_{\mathrm{signal}})t} \tag{12}$$

where $E_{b,0}$ and $E_{b,\pm1}$ are the complex amplitudes of the optical carrier and ±1-order sidebands, respectively. Next, by combining the optical signal of the two branches and performing balanced photodetection, an electrical signal carrying the frequency of f_{signal} can be generated, which is

$$i_{\mathrm{PD}}(t) = 2\eta\left(|E_a(t)|^2 - |E_b(t)|^2\right) - 2\mathrm{Re}\left[\eta j E_a(t) E_b^*(t)\right] \tag{13}$$

where η is the responsivity of the PDs. After being filtered by an LPF with a cutoff frequency of $f_s/4$, the useful part of the generated electrical signal can be extracted

$$\begin{aligned} i_{\mathrm{ADC}}(t) &= 2\mathrm{Re}\left[\eta j E_a(t) E_b^*(t)\right] \\ &= 2\eta E_{\mathrm{ADC}} \cos\left[2\pi(f_N - f_{\mathrm{signal}})t\right] \end{aligned} \tag{14}$$

where E_{ADC} is the complex amplitude of the electrical signal. It is worth noting that the shifted frequency f_{AOM} should be greater than $f_s/4$ to ensure that f_{AOM} can be effectively filtered out by the LPF. Consequently, an electrical power meter or an ADC can be performed to capture the power or amplitude changes when the CS-SSB optical signal is frequency sweeping. If $P(N)$ is the measured power or amplitude when $f_N = Nf_s/2 - f_s/4$, a notable change in $P(N)$ can be observed when f_{signal} falls within the Nth Nyquist band. Thus, the activated Nyquist bands of the unknown RF signal can be identified.

C. Sampling Pattern Optimization and Adaptive Control

In MCS, the condition number of the measurement matrix $\mathrm{cond}[\Phi_{p\times K}(f)]$ is determined by the sampling pattern. Moreover, the relative error of the solution obtained from (10) is proportional to the condition number. Therefore, careful design of the sampling pattern is the key to guarantee that the measurement matrix is well-conditioned. To simplify the analysis, two assumptions are made. First, the frequency response of the ith branch after demultiplexing, $H_{\mathrm{OE},i}(f)$, is assumed to be constant. Second, the spectral amplitude ratio of the optical pulses between the ith branch and the reference branch is assumed constant. Under these conditions, $A_i(nf_s, f)/A_1(nf_s, f) = A_i$, and the condition number of $\Phi_{p\times K}(f)$ can be given as (15), shown at the bottom of the page. According to (15), if the time delays after demultiplexing can be tuned to be equal,

$$\begin{cases} \mathbf{Y}_{p\times1}(f) \\ = \begin{bmatrix} Y_1(f) & Y_2(f) & \cdots & Y_p(f) \end{bmatrix}^{\mathrm{T}} \\ \Phi_{p\times K}(f) \\ = \begin{bmatrix} A_1(N_1f_s,f)e^{j\phi_1(N_1f_s,f)} & A_1(N_2f_s,f)e^{j\phi_1(N_2f_s,f)} & \cdots & A_1(N_Kf_s,f)e^{j\phi_1(N_Kf_s,f)} \\ A_2(N_1f_s,f)e^{j\phi_2(N_1f_s,f)} & A_2(N_2f_s,f)e^{j\phi_2(N_2f_s,f)} & \cdots & A_1(N_Kf_s,f)e^{j\phi_2(N_Kf_s,f)} \\ \vdots & \vdots & \ddots & \vdots \\ A_p(N_1f_s,f)e^{j\phi_p(N_1f_s,f)} & A_p(N_2f_s,f)e^{j\phi_p(N_2f_s,f)} & \cdots & A_p(N_Kf_s,f)e^{j\phi_p(N_Kf_s,f)} \end{bmatrix}, \quad f \in \left[0, \frac{f_s}{2}\right) \\ \mathbf{X}_{K\times1}(f) \\ = \left[X\left[\mathrm{ceil}\left(\frac{N_1-1}{2}\right)f_s + (-1)^{N_1-1}f\right] \; X\left[\mathrm{ceil}\left(\frac{N_2-1}{2}\right)f_s + (-1)^{N_2-1}f\right] \; \cdots \; X\left[\mathrm{ceil}\left(\frac{N_K-1}{2}\right)f_s + (-1)^{N_K-1}f\right] \right]^{\mathrm{T}} \end{cases} \tag{9}$$

$$\begin{cases} \mathrm{cond}\left[\Phi_{p\times K}(f)\right] = \mathrm{cond}\left[\mathbf{D}_1\Phi'_{p\times K}(f)\mathbf{D}_2(f)\right] \le \mathrm{cond}(\mathbf{D}_1)\cdot\mathrm{cond}\left[\Phi'_{p\times K}(f)\right] = \dfrac{\max(A_i)}{\min(A_i)}\mathrm{cond}\left[\Phi'_{p\times K}(f)\right] \\ \mathbf{D}_1 = \mathrm{diag}(A_1, A_2, \ldots, A_p) \\ \mathbf{D}_2(f) = \mathrm{diag}[e^{j\phi_1(N_1f_s,f)}, e^{j\phi_1(N_2f_s,f)}, \ldots, e^{j\phi_1(N_Kf_s,f)}], \quad \Phi'_{p\times K}(f) = \begin{bmatrix} 1 & 1 & \cdots & 1 \\ e^{j\Delta\phi_2(N_1f_s,f)} & e^{j\Delta\phi_2(N_2f_s,f)} & \ldots & e^{j\Delta\phi_2(N_Kf_s,f)} \\ \vdots & \vdots & \ddots & \vdots \\ e^{j\Delta\phi_p(N_1f_s,f)} & e^{j\Delta\phi_p(N_2f_s,f)} & \ldots & e^{j\Delta\phi_p(N_Kf_s,f)} \end{bmatrix} \end{cases} \tag{15}$$

cond[$\Phi'_{p\times K}(f)$] will be only determined by the activated Nyquist bands of the unknown RF signal $\{N_1, N_2, \ldots, N_K\}$ and the relative sampling pattern $\{0, \tau_2 - \tau_1, \ldots, \tau_p - \tau_1\}$. Therefore, to ensure the minimization of the condition number, the relative sampling pattern, the relative time delays after demultiplexing, $\{0, \tau'_2 - \tau'_1, \ldots, \tau'_p - \tau'_1\}$, and A_i should be measured and controlled.

First, the measurement matrix $\Phi_{p\times K}(f)$ can be established by employing a fine microwave frequency-sweeping method. In this case, the representations of $x(t)$ and $X(f)$ can be expressed as follows

$$\begin{cases} x(t) = a_0 \exp(j2\pi f_{\mathrm{RF}} t) \\ X(f) = a_0 \delta(f - f_{\mathrm{RF}}) \end{cases} \tag{16}$$

where a_0 denotes the complex amplitude, $f_{\mathrm{RF}} = \mathrm{ceil}[(n-1)/2]f_s + (-1)^{(n-1)} f_{\mathrm{IF}}$, n is the order index of the Nyquist bands, and f_{IF} is the IF between 0 and $f_s/2$. Then, the digitalized spectrum of the ith branch can be given as

$$Y_i(f_{\mathrm{RF}}) = a_0 A_i(nf_s, f_{\mathrm{RF}}) e^{j\phi_i(nf_s, f_{\mathrm{RF}})}. \tag{17}$$

Thus, the elements of the measurement matrix $\Phi_{p\times K}(f)$ can be obtained by sweeping the frequency f_{RF} and applying the fast Fourier transform (FFT) to extract the amplitude and phase of the digitalized signal. The ratio of the complex spectral amplitude between the ith branch and the reference branch can be given as

$$\frac{Y_i(f)}{Y_1(f)} = \frac{A_i(nf_s, f_{\mathrm{RF}}) e^{j\phi_i(nf_s, f_{\mathrm{RF}})}}{A_1(nf_s, f_{\mathrm{RF}}) e^{j\phi_1(nf_s, f_{\mathrm{RF}})}} = \tilde{A}_i(nf_s, f_{\mathrm{RF}}) e^{j\Delta\phi_i(nf_s, f_{\mathrm{RF}})}. \tag{18}$$

The relative phase shift $\Delta\phi_i$ can be written as

$$\Delta\phi_i(nf_s, f_{\mathrm{RF}}) = (-1)^{n-1} \left[2\pi \mathrm{ceil}\left(\frac{n-1}{2}\right) f_s \Delta\tau_i + 2\pi f_{\mathrm{IF}} \Delta\tau'_i \right]. \tag{19}$$

According to the IF-fixed frequency-sweeping method that we established in our previous work [29], the relative sampling pattern can be derived from the phase shifts of the frequencies $f_{\mathrm{RF}} = Nf_s + f_{\mathrm{IF}}$ $(N = 1, 2, \ldots, N)$

$$\Delta\tau_i = \frac{\Delta\phi_i(N_2 f_s, f_{\mathrm{RF}}) - \Delta\phi_i(N_1 f_s, f_{\mathrm{RF}})}{2\pi(N_2 - N_1) f_s}. \tag{20}$$

The relative time delay after demultiplexing can also be derived from the phase shifts of the frequencies within the first Nyquist band $f_{\mathrm{RF}} = f_{\mathrm{IF},i}$ $(i = 1, 2, \ldots, N)$

$$\Delta\tau'_i = \frac{\Delta\phi_i(0, f_{\mathrm{IF2}}) - \Delta\phi_i(0, f_{\mathrm{IF1}})}{2\pi(f_{\mathrm{IF2}} - f_{\mathrm{IF1}})}. \tag{21}$$

Next, after tuning the relative time delay after demultiplexing to zero, cond[$\Phi'_{p\times K}(f)$] is independent with f. Then, the condition number of $\Phi_{p\times K}(f)$ can be optimized by the minimization of cond($\Phi'_{p\times K}$), which can be modeled as

$$\Delta\tau_{\mathrm{opt}} = \arg \min_{\{\Delta\tau_2, \Delta\tau_3, \ldots, \Delta\tau_p\}} \mathrm{cond}\left(\Phi'_{p\times K}\right) \tag{22}$$

where $\Delta\tau_{\mathrm{opt}}$ is the optimized sampling pattern based on the prior spectral support of the unknown RF signal. After identifying the optimal $\Delta\tau_{\mathrm{opt}}$, the sampling pattern can be adjusted to minimize the condition number cond[$\Phi_{p\times K}(f)$] and $X(f)$ can be effectively reconstructed according to (10).

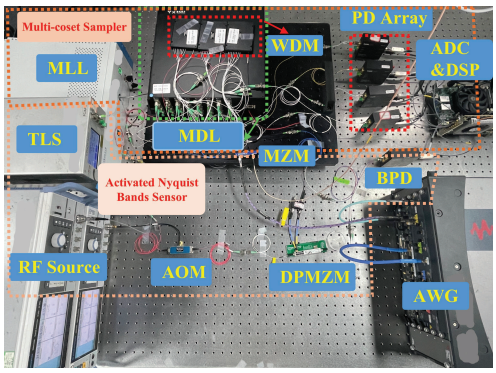

Fig. 4. Photograph of the experimental setup.

III. Experimental Results

A. Experimental Setup

To demonstrate the effectiveness of the proposed adaptive microwave-photonic MCS system, a proof-of-concept experiment was conducted based on the schematic of Fig. 3(a). To enhance clarity, Fig. 4 presents a photograph of the experimental setup. In the microwave photonic multi-coset sampler, a passive MLL was used to generate optical pulses with a repetition rate of 1 GHz and an optical power of 16 dBm. The generated optical pulses were then split into four branches by a polarization-maintaining wavelength division MUX (YiXun, YXWDM-15PM), corresponding to wavelengths C13, C19, C25, and C31. Polarization-maintaining motorized variable optical delay lines (MDL; YiXun, YXODL-15PM) with 5-fs resolution were placed after the MUX. These delay lines provided adjustable time delays, enabling flexible tuning of the sampling pattern. Afterward, the delayed optical pulses were recombined using another MUX arranged with reversed wavelength ordering to balance time delay differences caused by wavelength-dependent branches. Subsequently, the recombined optical pulses were directed into an MZM (Eospace, AX-0MVS-40), biased at its QTP, to perform optical sampling. Then, the sampled optical pulses were demultiplexed into four branches using another MUX, each passing through additional MDLs before detection by the PDs (Thorlab, PDB480C). It is worth noting that the MDLs employed here were used to adjust the time delays after demultiplexing. The resulting electrical signals from each PD were then filtered using LPFs (Talent Microwave, TLLF-DC-500M) with a cutoff frequency of 500 MHz and acquired by a multichannel data acquisition card (DAQ; Inspire, RFSoC 5008) with a sampling rate of 1 GSa/s and 14-bit resolution. The sampling clock of the DAQ was synchronized to the repetition rate of the MLL.

In the activated Nyquist band sensor, a TLS (ID Photonics, CoBrite-DX) was employed to emit a continuous wave at 1547.72 nm with an optical power of 16 dBm. The laser output was split into two branches using a 1 OC × 2 OC. One branch was combined with optical pulses via the MUX. The combined

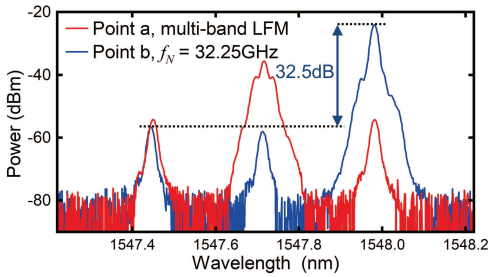

Fig. 5. Optical spectra of points a and b in Fig. 3.

optical signals were intensity-modulated by the same MZM and subsequently separated again using the DeMUX. The other branch was first frequency-shifted via an AOM (CETC, SGTF400-1550) driven by a 400-MHz RF signal, followed by the CS-SSB modulation implemented with a DPMZM (Fujitsu, FTM7961EX). The RF signal driving the DPMZM was provided by a microwave source (R&S, SMA100B) configured for frequency sweeping. The two branches were then combined via a 2 OC × 2 OC and detected by a balanced detector (BPD; Thorlab, PDB480C). After photodetection, the electrical signals were filtered by LPFs with a cutoff frequency of 250 MHz and collected using the multichannel DAQ. An arbitrary waveform generator (AWG; Keysight, M8199A) with a sampling rate of 128 GSa/s was utilized to generate the unknown multiband signal $x(t)$. To measure the sampling patterns and the measurement matrix, another programmable microwave source (R&S, SMA100B) provided the swept-frequency signal. In addition, all optical components used were polarization-maintaining, and all microwave sources were mutually synchronized. Instrument control, signal acquisition, and processing were managed centrally by a personal computer (PC).

B. Activated Nyquist Band Sensing of Multiband Signals

In the experiment on activated Nyquist band sensing, the AWG was used to generate linear frequency-modulated (LFM) pulses across four distinct frequency bands: 2.05–2.2, 2.8–2.95, 32.05–32.2, and 32.8–32.95 GHz. Each pulse had a duration of 1 μs, a period of 4 μs, and an amplitude of 280 mVpp. The generated signal was then applied to the MZM. The red curve in Fig. 5 shows the modulated optical spectra, measured using an optical spectrum analyzer (OSA; Yokogawa, AQ6370D). For comparison, the blue curve in Fig. 5 corresponds to the CS-SSB modulation obtained from the optical signal of the other branch. In this case, an AOM introduced a 400-MHz frequency shift, while a 32.29-GHz signal was applied to the DPMZM. A carrier-to-sideband ratio of 32.5 dB was achieved, effectively suppressing the unwanted beating components. Fig. 6 presents the digitized waveforms and their corresponding envelopes acquired by the ADCs, where the frequency of f_N was set to 1.75, 2.25, 2.75, 3.25, 31.75, 32.25, 32.75, and 33.25 GHz. The results indicate that when f_N falls within an activated Nyquist band, the useful signal can be successfully detected; otherwise, no signal is observed. It is also important to note that a complete digitized

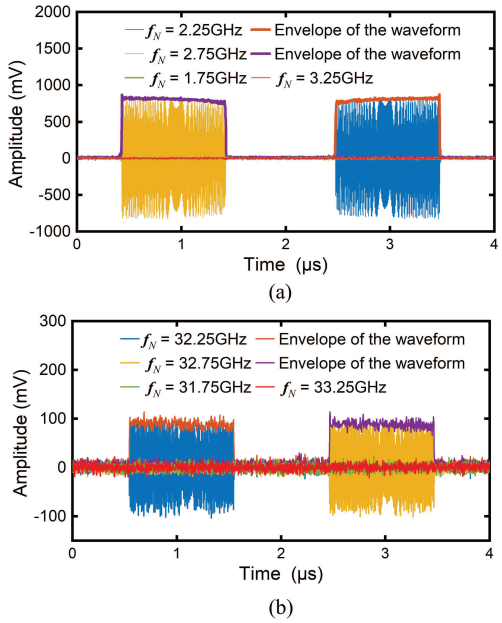

Fig. 6. Digitized waveforms and their corresponding envelopes acquired by the ADCs. (a) Setting f_N to 1.75, 2.25, 2.75, and 3.25 GHz. (b) Setting f_N to 31.75, 32.25, 32.75, and 33.25 GHz.

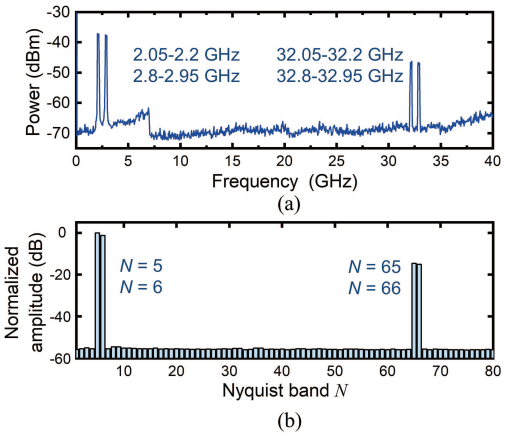

Fig. 7. (a) Spectrum of the LFM within 0.01–40 GHz. (b) Corresponding activated Nyquist band sensing results $P(N)$.

waveform is not required for the sensing of prior spectral support, and only the envelope information was utilized. The squared sum of the envelope corresponding to f_N is denoted as $P(N)$.

To further validate the proposed prior sensing approach, Fig. 7(a) and (b) illustrates the spectrum of the LFM within 0.01–40 GHz and the corresponding activated Nyquist band sensing results, respectively. The results in Fig. 7(b) exhibit strong agreement with the actual spectrum measured in Fig. 7(a). The spectrum in Fig. 7(a) was obtained using a spectrum analyzer (R&S, FSV) with a resolution bandwidth (RBW) of 50 kHz and a reference attenuation of 25 dB. These results confirm that the proposed activated Nyquist band sensing method can effectively determine the Nyquist bands distribution of an unknown multiband signal, thus providing

TABLE I
OPTIMIZED SAMPLING PATTERN AND CONDITION NUMBER

Activated Nyquist bands (N_1, N_2, …, N_K)	Optimized sampling pattern (ps) ($\Delta\tau_2$, $\Delta\tau_3$, …, $\Delta\tau_K$)	Condition number of $\mathbf{\Phi'}$
(5, 6, 65, 66)	(250, 500, 750)	1.0001
(5, 6, 65, 66)	(-416.7, 483.3, 700)	1.0007
(5, 6, 65, 66)	(50, 300, 950)	1.0024
(1, 6, 33, 76)	(35.9, 85.9, 842.9)	1.7600
(2, 6, 41, 76)	(71.4, 233.3, 304.8)	1.2248
(5, 6, 69, 70)	(-9.46, 362.8, 511.4)	1.5416
(5, 11, 34, 80)	(296.9, 500, 796.8)	1.1033
(5, 6, 21,33, 76)	(325.1, 443.6, 562, 887.1)	1.4705
(5, 6, 21,33, 48, 76)	(45.4, 487.2, 602.9, 738.5, 931.2)	1.8409

useful prior spectral support. Furthermore, the sensing resolution can be enhanced by adjusting the increment value of the frequency-sweeping signal and the cutoff bandwidth of the LPF. This aspect will be discussed in the following sections.

C. Sampling Pattern Measurement and Optimization

After acquiring the prior spectral information of the unknown multiband signal, the optimal sampling pattern was determined by solving (15), minimizing the condition number cond($\Phi'_{p\times K}$). A multistart search algorithm was employed to solve (15) in the experiment [30]. Table I presents the optimized sampling patterns identified after determining the activated Nyquist bands, along with the corresponding condition numbers of Φ'. The sampling rate f_s is fixed at 1 GSa/s. The results reveal that multiple distinct sampling patterns can yield low condition numbers for the same spectral prior. Notably, uniform sampling patterns rarely appear among the optimal solutions, further supporting the superiority of nonuniform sampling for multiband signals acquisition [31]. Once the optimal sampling pattern was obtained, the initial sampling pattern of the microwave photonic multi-coset sampler can be characterized using (16)–(21).

In the experiment, a frequency-sweeping microwave signal ranging from 0.01 to 39.01 GHz with a 1-GHz increment was applied. At each sweep, the ADCs captured an IF signal at 10 MHz. The amplitude and phase at 10 MHz were extracted via FFT. Then, the relative phase responses of the three branches with respect to the reference branch were obtained, as shown in Fig. 8(a). The relative time delays were derived from the linear regression of the relative phase responses, yielding an initial sampling pattern of {0, 182.13, 364.06, and 353.66 ps}. To characterize the relative time delays after demultiplexing, an additional frequency-sweeping microwave signal ranging from 20 to 420 MHz with a 5-MHz increment was performed. Fig. 8(b) shows the measured relative phase response, where a linear regression yielded relative delays of −4636.9, −7668.6, and −12616.1 ps, respectively. These results were then used to adjust the MDLs, ensuring alignment with the optimized sampling pattern.

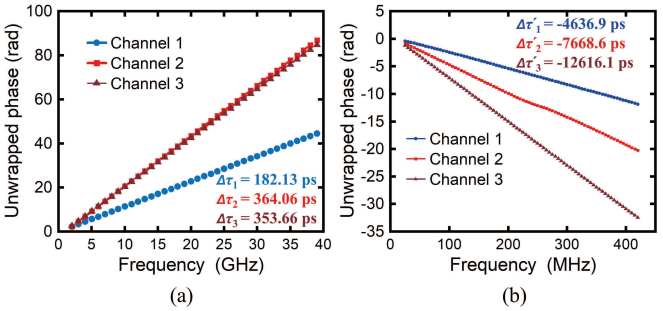

Fig. 8. Relative phase responses of the three branches with respect to the reference branch. (a) Relative phase response with frequency ranging from 0.01 to 39.01 GHz with a 1-GHz increment. (b) Relative phase response with frequency ranging from 20 to 420 MHz with a 5-MHz increment.

Next, to determine the measurement matrix $\Phi_{p\times K}(f)$ in (8), a fine-frequency-sweeping signal was applied to measure the relative amplitude and phase responses of multiple branches in the microwave photonic multi-coset sampler. The sweeping frequency was ranging from 0.01 to 39.01 GHz with a 10-MHz increment. The results are shown in Fig. 9.

Fig. 9(a) depicts the amplitude response of the reference channel (Channel 0), revealing a 6-dB bandwidth of approximately 40 GHz, which is constrained by the amplitude response of the MZM and the optical pulsewidth [32]. Fig. 8(b) and (c) illustrates the relative amplitude and phase responses for sampling patterns {0, 25, −250, and −500 ps}. The relative amplitude response remains nearly constant, validating the assumption proposed in the theoretical analysis. Notably, the system's relative phase response exhibits periodicity, with the period dictated by the sampling pattern. Additionally, discontinuities in the system response were observed at frequencies folded to $f_s/2$, likely due to the amplitude response fading of the LPF.

Fig. 10(a)–(d) depicts the relative amplitude and phase responses of the 5th, 6th, 65th, and 66th Nyquist bands for sampling patterns {0, −250, 500, and 750 ps}, respectively. The results indicate that the relative response remains nearly constant across each Nyquist band, particularly in the phase response, thanks to the precise tuning of time delays after demultiplexing. Fig. 11 shows the condition number of the measurement matrix $\Phi_{p\times K}(f)$, derived from the relative amplitude and phase responses of Nyquist bands 5, 6, 65, and 66. The results reveal that, apart from the frequency around 500 MHz, the condition number remains consistently low at approximately 1.9.

D. Sampling and Reconstruction of Multiband RF Signals Spanning Four Nyquist Bands

After acquiring the prior spectral support of the unknown multiband signal and optimizing the sampling pattern of

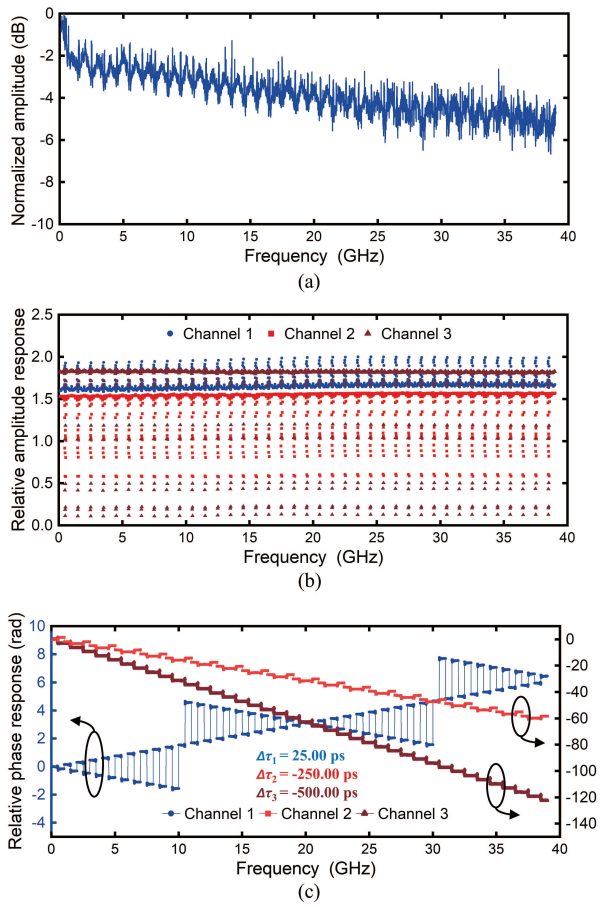

Fig. 9. (a) Amplitude response of the reference channel. (b) Relative amplitude responses and (c) relative phase responses of the three channels with respect to the reference channel with frequency ranging from 0.01 to 39.01 GHz with a 10-MHz increment.

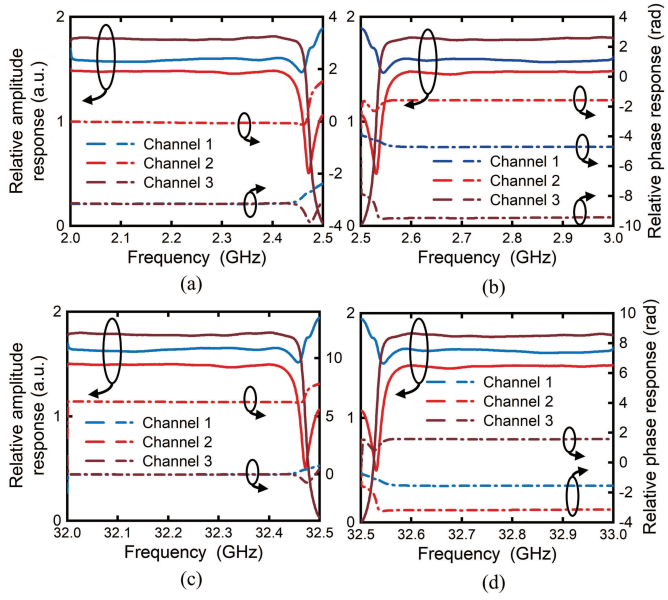

Fig. 10. Relative amplitude and phase responses of different Nyquist bands. (a) 5th Nyquist band. (b) 6th Nyquist band. (c) 65th Nyquist band. (d) 66th Nyquist band.

the microwave photonic multi-coset sampler, the signal can be sampled and reconstructed. A multiband signal spanning

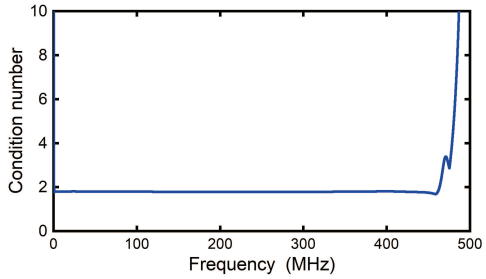

Fig. 11. Condition number of the measurement matrix $\Phi_{p\times K}(f)$, derived from the relative amplitude and phase responses of Nyquist bands 5, 6, 65, and 66.

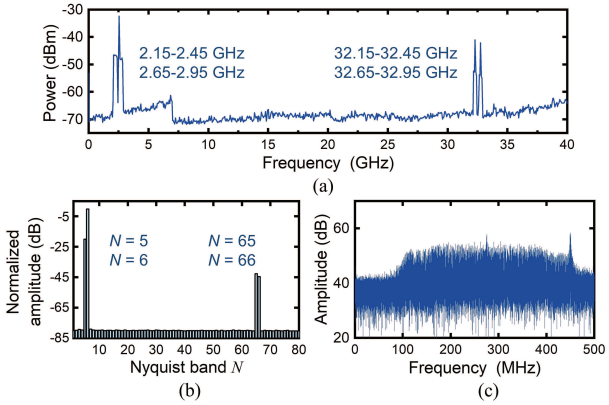

Fig. 12. (a) Spectrum obtained from the spectrum analyzer. (b) Spectral sensing results obtained from the proposed activated Nyquist band sensor. (c) Digitized spectrum from one channel of the microwave photonic multi-coset sampler.

TABLE II
PARAMETERS OF THE MULTIBAND RF SIGNAL

Signal type	Frequency range (GHz)	Time window (μs)
Up-chirp LFM	(2.1, 2.4)	(0,0.33), (0.66, 1)
	(2.55, 2.85)	(0, 0.5), (0.5, 1)
	(32.15-32.4)	(1, 1.5)
	(32.6-32.85)	(2,2.5)
Down-chirp LFM	(2.1, 2.4)	(0.33, 0.66)
	(32.15-32.4)	(1.5, 2)
	(32.6-32.85)	(2.5, 3)
Single tone	2.55	(0, 0.5)
	32.375	(1.25,1.75)
	32.725	(2.25,2.75)

Nyquist bands of 5, 6, 65, and 66 was generated using the AWG. The signal had a 4-μs period, with its waveform characteristics and time–frequency parameters summarized in Table II. Fig. 12(a) and (b) presents the spectral sensing

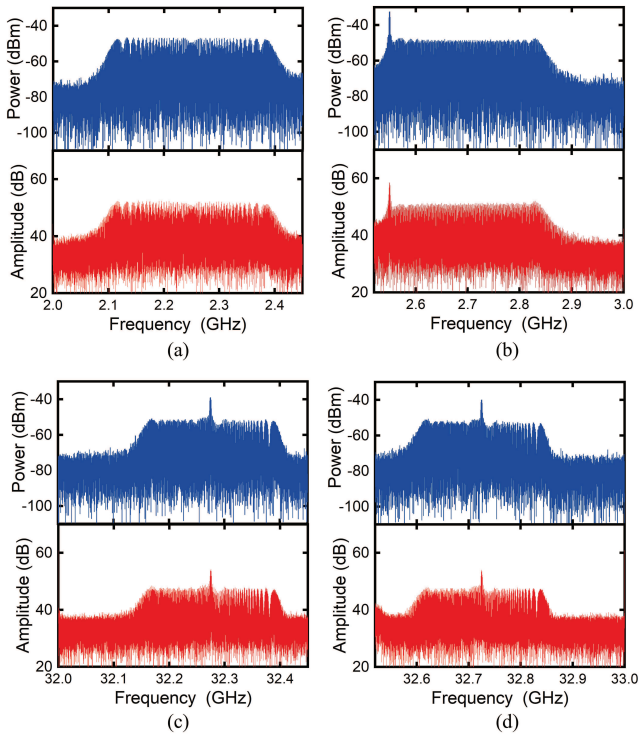

Fig. 13. Spectra measured by the spectrum analyzer (blue curve) and reconstructed by the proposed method (red curve). (a) 2–2.5 GHz, (b) 2.5–3 GHz, (c) 32–32.5 GHz, and (d) 32.5–33 GHz.

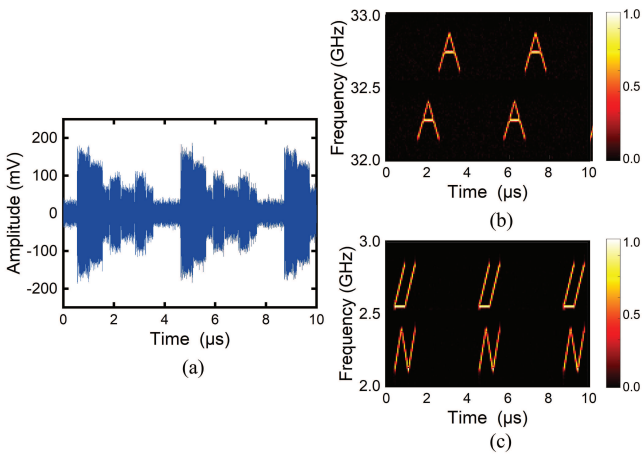

Fig. 14. (a) Time-domain waveform of the reconstructed signal, upsampled to 80 GSa/s. (b) Time–frequency representations for 32–33 GHz. (c) Time–frequency representations for 2–3 GHz.

results obtained from the spectrum analyzer and the proposed activated Nyquist band sensor, respectively.

The results confirm the successful identification of occupied Nyquist bands. Fig. 12(c) displays the digitized spectrum from one channel of the microwave photonic multi-coset sampler over a 10-μs data window. It is observed that all spectral components were folded into the first Nyquist band.

In Fig. 13, the blue curves represent the spectrum measured by a spectrum analyzer, with a span of 500 MHz and the red curves correspond to the reconstructed spectrum obtained using (10), covering four Nyquist bands with frequency ranges of 2–2.5, 2.5–3, 32–32.5, and 32.5–33 GHz. Fig. 14(a) shows

TABLE III
PARAMETERS OF THE MULTIBAND RF SIGNAL

Signal type	Frequency range (GHz)	Time window (μs)
Up-chirp LFM	(2.1, 2.24)	(0, 0.5)
	(14.8, 14.925)	(0.5, 1)
	(31.6, 31.74)	(2, 2.5)
	(39.75, 39.9)	(2.5, 3)
Down-chirp LFM	(6.25, 6.4)	(0.5, 1)
	(10.6, 10.74)	(0, 0.5)
	(23.1, 23.24)	(1, 1.5)
	(27.25, 27.4)	(1.5, 2)

the time-domain waveform of the reconstructed signal, upsampled to 80 GSa/s. Fig. 14(b) and (c) depicts the time–frequency representations of the signal over a 10-μs window for the frequency ranges 32–33 and 2–3 GHz, respectively. The results demonstrate that the proposed method successfully reconstructed the multiband signal and effectively separated the folded spectral components from the four Nyquist bands, overcoming the frequency aliasing limitations of sub-Nyquist sampling.

E. Sampling and Reconstruction of Multiband RF Signals Spanning Eight Nyquist Bands

As shown in (15), for K activated Nyquist bands, the uniform sampling pattern can serve as an optimized uniform sampling pattern when the activated Nyquist bands follow the form $\{Kn_1 + 1,\ Kn_2 + 2,\ Kn_3 + 3, \ldots, Kn_K + K\}$, where n_1, $n_2, \ldots, n_K \in \mathbb{N}_0$. In this case, the sampling pattern is given by $\{0,\ T_s/K,\ 2T_s/K, \ldots, (K-1)T_s/K\}$, where T_s denotes the sampling period. Under such conditions, the relative amplitude response remains approximately constant within the Nyquist bandwidth, and the relative phase response exhibits periodicity with a period of Kf_s. As a result, it is sufficient to measure the relative response only within the first K Nyquist bands, from which the response in all activated bands can be inferred.

To verify the applicability of the proposed method in scenarios discussed above, an eight-band signal was sampled and reconstructed using a four-channel adaptive microwave MCS system. The signal characteristics and time–frequency parameters are summarized in Table III. As can be seen, while the effective bandwidth remains around 2 GHz, the signal spans eight Nyquist bands.

To enhance spectral sensing resolution, the frequency-sweeping increment of the prior spectral sensor was set to be 250 MHz, and the cutoff frequency of the LPF was adjusted to 125 MHz. Under these conditions, the sensor achieved finer prior spectral estimation. Fig. 15(a) and (b) presents the spectrum obtained from a spectrum analyzer and the estimated

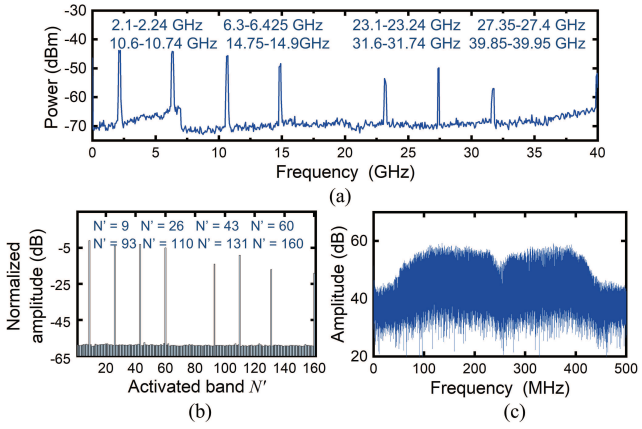

Fig. 15. (a) Spectrum obtained from the spectrum analyzer. (b) Spectral sensing results obtained from the proposed prior spectral sensor. (c) Digitized spectrum from one channel of the microwave photonic multi-coset sampler.

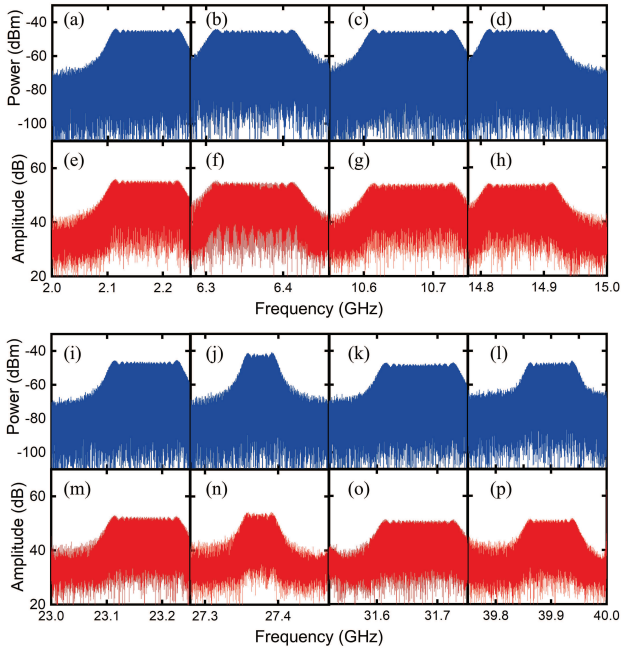

Fig. 16. (a)–(d) and (i)–(l) Spectra measured by the spectrum analyzer (blue curve). (e)–(h) and (m)–(p) Reconstructed spectra by the proposed method (red curve).

prior spectral support, respectively. The results indicate that the 40-GHz bandwidth was divided into 160 bins based on the sweep increment, and the occupied spectral bins were successfully identified to be {9, 26, 43, 60, 93, 110, 131, 160}. Therefore, the signal was found to occupy Nyquist bands 5, 13, 22, 30, 47, 55, 64, and 80.

By exploiting the periodicity of the relative amplitude and phase responses of the sampling system, it was observed that the responses in Nyquist bands 13, 30, 55, and 80 were identical to those in bands 5, 22, 47, and 64, respectively, which in turn matched the responses in Nyquist bands 1, 2, 3, and 4. Consequently, measuring the responses in only first four Nyquist bands was sufficient for signal reconstruction.

Fig. 15(c) presents the digitized spectrum obtained from one channel of the microwave photonic multi-coset sampler, corresponding to a 10-μs data window. Figs. 16 and 17

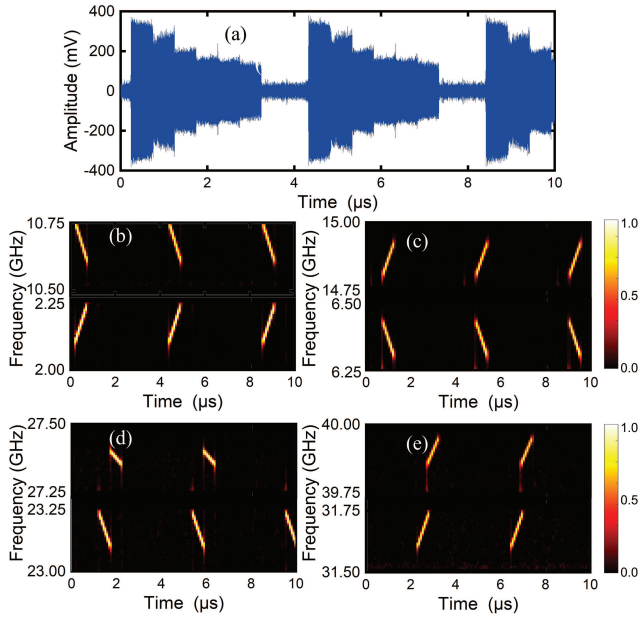

Fig. 17. (a) Time-domain waveform of the reconstructed signal, upsampled to 80 GSa/s. (b) Time–frequency representations for 2–2.25 and 10.5–10.75 GHz. (c) 6.25–6.5 and 14.75–15 GHz. (d) 23–23.25 and 27.25–27.5 GHz. (e) 31.5–31.75 and 39.75–40 GHz.

illustrate the reconstructed time-domain, frequency-domain, and time–frequency representations of the signal. The results confirm that the signal was successfully reconstructed.

IV. Discussion

In the proposed microwave photonic multi-coset sampler, the reconstruction performance is determined by the condition number of the measurement matrix, which in turn depends on the sampling pattern. Therefore, the choice of sampling pattern and the associated setting errors play a critical role in signal reconstruction. Fig. 18(a) compares the condition numbers of uniform and nonuniform sampling patterns when the activated Nyquist bands are 5, 6, 69, and 70. The results indicate that for the uniform sampling pattern, the condition number remains around 173. In the experiments, this high condition number led to signal reconstruction failure. In contrast, the nonuniform sampling pattern derived from (22) achieves a significantly lower condition number of approximately 1.8, primarily constrained by optical power differences between channels, and successful signal reconstruction was achieved when the optimal nonuniform sampling pattern was employed. Fig. 18(b) illustrates the variation in the condition number caused by time delay fluctuations in two channels when the four adjacent Nyquist bands are activated. The results reveal that for a contiguously distributed multiband signal, the optimal sampling pattern can be either uniform or nonuniform. In the uniform sampling case, the condition number of the measurement matrix remains insensitive to time delay errors. However, for nonuniform sampling, the condition number is more sensitive to time delay variations, highlighting the importance of precise time delay measurement and calibration in the system.

Table IV provides a comparative summary of state-of-the-art multiband RF front-end designs employed in multiband radar

TABLE IV
COMPARISON WITH STATE-OF-THE-ART MULTIBAND RF FRONT-END DESIGNS

Application	Methods	$\frac{SR}{2\times CB}$	Operating bandwidth	Spectral aliasing mitigation methods	Adaptability
Multi-band radar	Multi-channel LO receiver [2]	2	0-40 GHz	Anti-aliasing filter	No
	Channelizer [34]	>8	0-40 GHz	Anti-aliasing filter	No
Spectrum sensing	Frequency scanning [35]	—	2-22 GHz	Anti-aliasing filter	No
	Photonic Fourier transform [36]	>1	0-40 GHz	High sampling rate	No
Cognitive radio	Compressed sensing [3]	>20	11-41 GHz	Anti-aliasing filter	Yes
	Direct RF sampling [37]	>1	0-13 GHz	Anti-aliasing filter	Yes
This work	**Adaptive MCS**	**~1**	**0.01-40GHz**	**Filterless Low sampling rate**	**Yes**

SR: Sampling rate; CB: Cumulative bandwidth.

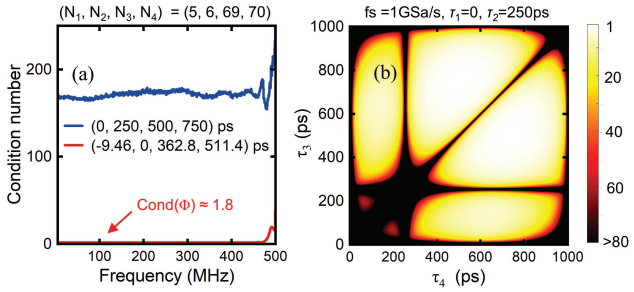

Fig. 18. (a) Condition numbers of uniform and nonuniform sampling patterns when the activated Nyquist bands are 5, 6, 69, and 70. (b) Variation in the condition number caused by time delay fluctuations in two channels when the first four adjacent Nyquist bands are activated.

[2], [33], [34], spectrum sensing [35], [36], and cognitive radio applications [3], [37]. It is evident that most approaches can not reach the minimum sampling rate when the signal occupies noncontiguous frequency bands. Critically, most existing methods rely on anti-aliasing filters or high sampling rates to prevent spectral aliasing. These solutions typically require numerous downconversion channels, introduce substantial sampling redundancy, or cannot simultaneously capture complete time-domain information across all frequency bands. Moreover, once filter parameters are fixed, the system loses adaptability to dynamic spectral environments. In contrast, the proposed method employs sub-Nyquist sampling combined with prior spectral knowledge to reconstruct the original time-domain signal directly from aliased samples. This approach eliminates the need for filter banks, achieves minimal sampling rates, and inherently supports adaptive operation.

V. CONCLUSION

In conclusion, an adaptive microwave-photonic MCS method has been proposed and experimentally demonstrated, offering a hardware-efficient and high-fidelity solution for sub-Nyquist acquisition of multiband RF signals. The system integrates an activated Nyquist band sensor with fine-grained microwave frequency sweeping to estimate the prior spectral support and accurately measure both the sampling pattern and the measurement matrix. Based on this prior knowledge, the sampling pattern is optimized to minimize the condition number, ensuring robust signal reconstruction even under aliasing constraints. A four-channel 1-GSa/s MCS system has been implemented, achieving successful reconstruction of multiband signals spanning four and eight Nyquist bands across the entire 0.01–40-GHz range, with a cumulative bandwidth of 2 GHz. Furthermore, the proposed approach demonstrates strong resilience to spectral aliasing, supports sampling pattern optimization, and enables the use of minimal sampling rate. This work, to the best of our knowledge, represents the first adaptive microwave-photonic MCS system featuring full-band spectral sensing and sampling pattern control. The architecture is compact, modular, and composed entirely of integrable components. We believe that this system provides a powerful and scalable foundation for advanced multiband RF front-end designs. It holds significant promise for enabling next-generation applications in multiband radar, wideband spectrum sensing, and cognitive radio.

REFERENCES

[1] M. Skolnik, *Radar Handbook*, 3rd ed., New York, NY, USA: McGraw-Hill, 2008.
[2] G. Serafino et al., "Toward a new generation of radar systems based on microwave photonic technologies," *J. Lightw. Technol.*, vol. 37, no. 2, pp. 643–650, Jan. 15, 2019.
[3] J. A. Zhang et al., "Enabling joint communication and radar sensing in mobile networks—A survey," *IEEE Commun. Surveys Tuts.*, vol. 24, no. 1, pp. 306–345, 1st Quart., 2022.
[4] X. Chen et al., "Versatile photonic-assisted cognitive radio regulatory system employing joint collaboration of multiple photonic integrated chips," *J. Lightw. Technol.*, vol. 42, no. 10, pp. 3592–3600, May 10, 2024.

[5] M. Horlbeck, T. Kurin, B. Scheiner, R. Weigel, and F. Lurz, "Design of a super heterodyne receiver with double conversion for passive radar with FM radio," in *Proc. Asia Pacific Microw. Conf. (APMC)*, Dec. 2023, pp. 378–380.

[6] A. Schuster, G. Fischer, R. Weigel, and T. Reissland, "Towards spectrum sensing within 6th generation mobile communications in the sub-6 GHz frequency range using wideband direct sampling architectures," in *IEEE MTT-S Int. Microw. Symp. Dig.*, San Juan, PR, USA, Jan. 2025, pp. 70–73.

[7] D. Cohen, S. Tsiper, and Y. C. Eldar, "Analog-to-digital cognitive radio: Sampling, detection, and hardware," *IEEE Signal Process. Mag.*, vol. 35, no. 1, pp. 137–166, Jan. 2018.

[8] J. Yang, Z. Song, Y. Gao, X. Gu, and Z. Feng, "Adaptive compressed spectrum sensing for multiband signals," *IEEE Trans. Wireless Commun.*, vol. 20, no. 11, pp. 7642–7654, Nov. 2021.

[9] J. A. Tropp, J. N. Laska, M. F. Duarte, J. K. Romberg, and R. G. Baraniuk, "Beyond nyquist: Efficient sampling of sparse bandlimited signals," *IEEE Trans. Inf. Theory*, vol. 56, no. 1, pp. 520–544, Jan. 2010.

[10] M. Mishali and Y. C. Eldar, "From theory to practice: Sub-nyquist sampling of sparse wideband analog signals," *IEEE J. Sel. Topics Signal Process.*, vol. 4, no. 2, pp. 375–391, Apr. 2010.

[11] M. Mishali and Y. C. Eldar, "Blind multiband signal reconstruction: Compressed sensing for analog signals," *IEEE Trans. Signal Process.*, vol. 57, no. 3, pp. 993–1009, Mar. 2009.

[12] F. Marvasti, *Nonuniform Sampling. in Information Technology: Transmission, Processing, and Storage*. Boston, MA, USA: Springer, 2001.

[13] Z. Song, X. Zhang, Z. Chen, R. Tafazolli, and Y. Gao, "GBSense: A GHz-bandwidth compressed spectrum sensing system," *IEEE Trans. Circuits Syst. I, Reg. Papers*, early access, Jan. 27, 2025, doi: 10.1109/TCSI.2025.3530259.

[14] Z. Song, J. Yang, H. Zhang, and Y. Gao, "Approaching sub-nyquist boundary: Optimized compressed spectrum sensing based on multicoset sampler for multiband signal," *IEEE Trans. Signal Process.*, vol. 70, pp. 4225–4238, 2022.

[15] J. Dong, H. Li, Z. Fan, and X. Zhao, "Time-frequency sparse reconstruction of non-uniform sampling for non-stationary signal," *IEEE Trans. Veh. Technol.*, vol. 70, no. 11, pp. 11145–11153, Nov. 2021.

[16] M. Mishali and Y. C. Eldar, "Wideband spectrum sensing at sub-nyquist rates [applications corner]," *IEEE Signal Process. Mag.*, vol. 28, no. 4, pp. 102–135, Jul. 2011.

[17] Z. Song, Y. She, J. Yang, J. Peng, Y. Gao, and R. Tafazolli, "Nonuniform sampling pattern design for compressed spectrum sensing in mobile cognitive radio networks," *IEEE Trans. Mobile Comput.*, vol. 23, no. 9, pp. 8680–8693, Sep. 2024.

[18] M. E. Domínguez-Jiménez, N. González-Prelcic, G. Vazquez-Vilar, and R. López-Valcarce, "Design of universal multicoset sampling patterns for compressed sensing of multiband sparse signals," in *Proc. IEEE Int. Conf. Acoust., Speech Signal Process. (ICASSP)*, Kyoto, Japan, Mar. 2012, pp. 3337–3340.

[19] B. Tausiesakul and N. Gonzalez-Prelcic, "Power spectrum blind sampling using optimal multicoset sampling patterns in the MSE sense," in *Proc. IEEE Int. Conf. Acoust., Speech Signal Process. (ICASSP)*, Florence, Italy, May 2014, pp. 1055–1059.

[20] R. Sharma, R. Shrestha, and S. K. Sharma, "Hardware-efficient and short sensing-time multicoset-sampling based wideband spectrum sensor for cognitive radio network," *IEEE Trans. Circuits Syst. I, Reg. Papers*, vol. 70, no. 3, pp. 1298–1310, Mar. 2023.

[21] X. Zou, B. Lu, W. Pan, L. Yan, A. Stöhr, and J. Yao, "Photonics for microwave measurements," *Laser Photon. Rev.*, vol. 10, no. 5, pp. 711–734, Sep. 2016.

[22] S. Pan and J. Yao, "Photonics-based broadband microwave measurement," *J. Lightw. Technol.*, vol. 35, no. 16, pp. 3498–3513, Aug. 15, 2017.

[23] S. Li, T. Qing, J. Fu, X. Wang, and S. Pan, "High-accuracy and fast measurement of optical transfer delay," *IEEE Trans. Instrum. Meas.*, vol. 70, pp. 1–4, 2021.

[24] P. Ghelfi et al., "A fully photonics-based coherent radar system," *Nature*, vol. 507, no. 7492, pp. 341–345, Mar. 2014.

[25] X. Li, A. Wen, X. Li, and J. Zhao, "Wideband RF subsampling and disambiguation based on phase shift analysis," *J. Lightw. Technol.*, vol. 40, no. 4, pp. 1027–1035, Feb. 4, 2022.

[26] L. Wang, X. Wang, and S. Pan, "Microwave photonics empowered integrated sensing and communication for 6G," *IEEE Trans. Microw. Theory Techn.*, early access, Feb. 4, 2025, doi: 10.1109/TMTT.2025.3532810.

[27] T. P. McKenna, J. H. Kalkavage, M. D. Sharp, and T. R. Clark, "Wideband photonic compressive sampling system," *J. Lightw. Technol.*, vol. 34, no. 11, pp. 2848–2855, Jun. 12, 2016.

[28] W. Dai et al., "Wideband spectrum compressive sensing utilizing photonic multi-coset sampling with dual low-rate optical pulses," *Appl. Opt.*, vol. 63, no. 18, pp. 4914–4919, Jun. 2024.

[29] X. Tang, Y. Zhang, L. Wang, K. Shao, P. Li, and S. Pan, "Multi-channel sampling time delay measurement and control for time-wavelength interleaved photonic analog-to-digital converters," in *Proc. Int. Topical Meeting Microw. Photon. (MWP)*, Nanjing, China, Oct. 2023, pp. 1–4.

[30] Z. Ugray, L. Lasdon, J. Plummer, F. Glover, J. Kelly, and R. Martí, "Scatter search and local NLP solvers: A multistart framework for global optimization," *INFORMS J. Comput.*, vol. 19, no. 3, pp. 328–340, Aug. 2007.

[31] R. Venkataramani and Y. Bresler, "Perfect reconstruction formulas and bounds on aliasing error in sub-nyquist nonuniform sampling of multiband signals," *IEEE Trans. Inf. Theory*, vol. 46, no. 6, pp. 2173–2183, Sep. 2000.

[32] B. C. Pile and G. W. Taylor, "Performance of subsampled analog optical links," *J. Lightw. Technol.*, vol. 30, no. 9, pp. 1299–1305, May 6, 2012.

[33] S. Pan and Y. Zhang, "Microwave photonic radars," *J. Lightw. Technol.*, vol. 38, no. 19, pp. 5450–5484, Oct. 19, 2020.

[34] W. Chen, D. Zhu, J. Liu, and S. Pan, "Multi-band RF transceiver based on the polarization multiplexed photonic LOs and mixers," *IEEE J. Sel. Topics Quantum Electron.*, vol. 27, no. 2, pp. 1–9, Mar. 2021.

[35] L. Zhong, M. Abbasi, S. M. A. Uddin, and W. Lee, "Broadband frequency-domain analog processor for spectrum sensing with 20 GHz scan range," *IEEE Trans. Circuits Syst. II, Exp. Briefs*, vol. 70, no. 5, pp. 1759–1763, May 2023.

[36] D. Zhu et al., "Microwave photonic cognitive radar with a subcentimeter resolution," *IEEE Trans. Microw. Theory Techn.*, vol. 72, no. 9, pp. 5519–5529, Sep. 2024.

[37] S. Henthorn, T. O'Farrell, M. R. Anbiyaei, and K. L. Ford, "Concurrent multiband direct RF sampling receivers," *IEEE Trans. Wireless Commun.*, vol. 22, no. 1, pp. 550–562, Jan. 2023.